

MEASURING GALAXY CLUSTERING AND THE EVOLUTION OF [CII] MEAN INTENSITY WITH FAR-IR LINE INTENSITY MAPPING DURING $0.5 < z < 1.5$

B. D. UZGIL^{1,2}, J. E. AGUIRRE¹, AND C. M. BRADFORD²

Draft version March 25, 2014

ABSTRACT

We explore the possibility of studying the redshifted [CII] fine structure transition through cosmic time using the three-dimensional (3D) power spectra obtained with an imaging spectrometer. The intensity mapping approach measures the spatio-spectral fluctuations due to line emission from all galaxies, including those below the individual detection threshold. This technique not only provides 3D measurements of galaxy clustering, but contains astrophysical information—namely, the average intensity of total [CII] emission—which can be extracted from the linear portion of the power spectrum, with redshift information naturally encoded. We further compare the intensity mapping approach to galaxy surveys comprised of individually detected galaxies, and find that intensity mapping provides an unbiased estimate of the mean [CII] intensity. Depending on the noise level of a given experiment, intensity mapping may provide the only means of measuring this aggregate quantity. Also, depending on the shape of the luminosity function, intensity mapping can be a more efficient means of measuring the power spectrum.

Keywords: far-infrared spectroscopy; galaxy redshift surveys

1. INTRODUCTION

Various observational techniques in astronomy, including, but not limited to, photometric and spectroscopic stacking analysis, “P(D)” fluctuation analysis, and recently, cosmological spectral deconvolution (cf. Dole et al. (2006); Glenn et al. (2010); de Putter et al. (2014) for examples of each), have been developed to provide a means to study the nature of galaxies that are otherwise too faint to be detected individually at high significance. These methods, which aim to maximize the information in low signal-to-noise datasets, rely heavily on interpreting the statistical and aggregate properties of the extragalactic sources, and yet the insight they have provided into the nature of galaxies and their evolution with cosmic time has been invaluable.

Line intensity mapping, also known as, simply, intensity mapping, or 3-D tomographic mapping, is one such technique that allows astronomers to probe extragalactic populations beyond their brightest sources. An intensity mapping survey of a spectral line at different frequencies produces a *fully three dimensional data cube containing “tomographic scans” of the Universe along the spectral (i.e., redshift) direction*. The spatial fluctuations in spectral line emission, contained in the data cube, are then decomposed into the power spectrum. Atomic (Gong et al. 2012; Visbal et al. 2011) and molecular (Lidz et al. 2011; Gong et al. 2011) transitions – such as the 21 cm spin flip transition from H⁰, CO (2-1), and [CII] 158 μ m – have been investigated as candidates for intensity mapping experiments during the Epoch of Reionization. Of these, the neutral hydrogen case is undoubtedly the most developed in terms of its standing in the literature (cf. Morales & Wyithe (2010) for a review) and in the experimental arena (e.g., PAPER (Parsons et al. 2013), MWA (Tingay et al. 2013)), and so interest in measuring the

[CII] power spectrum, for instance, primarily erupted as a means to complement the 21 cm studies at high redshift via the cross-correlation.

As a proof of principal, the appeal of intensity mapping experiments in the post-Reionization era is obvious. Neutral hydrogen is, again, the most mature in this respect, as 21cm experiments have successfully measured the 21cm-galaxy cross power spectrum (Chang et al. 2011) or put limits on the 21cm auto-power (Switzer et al. 2013), but the detectability of another Hydrogen transition, the Ly α line, has also been explored in (Pullen et al. 2013) et al for redshifts after Reionization down to $z \sim 2$.

Here we examine the application of the intensity mapping technique to moderate redshifts, targeting the fine structure line emission from ionized carbon in the inter-stellar medium of star-forming galaxies during $0.5 < z < 1.5$. The [CII]158 μ m line is a well-suited probe of the galaxy population during this time frame, as the mean dust attenuation in galaxies peaks at $z \sim 1.5$, when roughly 80% of the cosmic star formation rate density is obscured and captured only in the infrared emission of re-processed starlight by dust grains (Burgarella et al. 2013). Moreover, this line is typically the brightest FIR emitted from the ISM of galaxies, with luminosities up to 0.1% of the IR luminosity, and is an important signpost of star formation and related dynamics in galaxies Graciá-Carpio et al. (2011); Sargsyan et al. (2012); Díaz-Santos et al. (2013).

Due to the spatio-spectral nature of intensity mapping, this technique as applied to [CII] line intensity fluctuations can be a highly complementary probe to recent studies of the 2-dimensional clustering properties of dusty, star-forming galaxies (DSFGs) (see Casey et al. 2014 for a review). These studies, using a modification of the “P(D)” approach, for example by (Béthermin et al. 2011; Viero et al. 2012), have already shed light on some aspects of the clustering of the most extreme star-forming

badeu@sas.upenn.edu

¹ University of Pennsylvania, Philadelphia, PA 19104

² Jet Propulsion Laboratory

system from $z = 1 - 3$, but they are limited by the lack of redshift information, and by the need to include “nuisance parameters” in their estimation of the halo model. From the far-IR to the millimeter, it remains for the future for ALMA or NOEMA to produce redshift surveys with $\sim 10^3$ galaxies, or even further down the road for CCAT. Thus we present a novel method of characterizing the 3D clustering of DSFGs with [CII] intensity mapping, which, importantly, does not rely on detecting individual galaxies in order to measure the power spectrum with high significance.

Furthermore, this sensitivity of the power spectrum to galaxies which are below the threshold for individual detections by current and future instruments—paired with the fact that the amplitude of the power spectrum is proportional on large scales to the mean intensity of the target line—introduces additional astrophysically interesting information inherent in the intensity mapped data. Namely, by extracting the mean intensity of [CII], or any emission line of interest, from the power spectrum at a number of observed frequencies, intensity mapping provides a means of quantifying the aggregate luminosity from all [CII]-emitting sources at a given redshift. An example of using the power spectrum to determine luminosity density can be found in Planck Collaboration et al. (2013), although the results discussed there were derived from the 2-D angular power spectrum of IR continuum fluctuations, which relies on fits which include uncertainties in the dust spectral energy distributions, for instance. With inherent redshift information from the spectral line, such an observation of the 3-D power spectrum would ascertain the cosmic evolution of the Universe’s total output in [CII] with a level of precision not available by other means.

The organization of this paper is as follows. We have calculated the mean intensity for a suite of fine structure IR emission lines, including the [CII] line, based on the IR luminosity function and empirical line-to-IR luminosity correlations, and present these results in the context of a power spectrum model in Section 2. In Section 3, we envision a suitable platform—namely, a balloon-borne experiment operating at frequencies between $240\mu\text{m}$ to $420\mu\text{m}$ —for conducting the [CII] intensity mapping experiment and discuss the feasibility of detecting the [CII] power spectra in terms of the Signal-to-Noise Ratio. From the power spectra, we provide estimates for accuracy on measuring the mean [CII] intensity as a function of redshift. To better assess the value of intensity mapping studies in the case of [CII] at moderate redshifts, and of intensity mapping experiments in general, we compare in Section 4 the performance of the intensity mapping approach against spectroscopic galaxy surveys that rely on individual detections of sources to measure the power spectrum. In particular, we examine the effects of variations in luminosity function shape, aperture diameter (and, consequently, pixel size), and experimental noise on the ability of each observational method to measure the power spectrum and provide a complete view of the galaxy population.

2. SETTING UP PREDICTIONS FOR FAR-IR LINE POWER SPECTRA DURING $0.5 < Z < 3$

Conventional methods for measuring the spatial autocorrelation of galaxies through galaxy surveys rely on

the knowledge of the redshift distribution of sources in the survey. Furthermore, they estimate the true three dimensional clustering of galaxies via the angular projection. Intensity mapping, however, contains intrinsic redshift information and provides a direct measure of the clustering power spectrum in three-dimensional k-space, which makes it a highly complementary probe of structure in the cosmic web.

The complete auto power spectrum of a given FIR line as a function of wavenumber k , $P_{i,i}(k, z)$, can be separated into power from the clustering of galaxies, $P_{i,i}^{clust}(k, z)$ and a Poisson term describing their discrete nature, $P_{i,i}^{shot}(z)$. We compute the full nonlinear matter power spectrum, $P_{\delta\delta}(k, z)$, using the publicly available code HALOFIT+ (<http://camb.info>), which has been the standard tool for predicting matter power spectra upon its success in fitting state-of-the-art dark matter simulations over a decade ago (Smith et al. 2003). The clustering component of the line power spectrum is then written as

$$P_{i,i}^{clust}(k, z) = \bar{S}_i^2(z) \bar{b}_i^2(z) P_{\delta\delta}(k, z). \quad (1)$$

Here we have implicitly assumed that the fluctuations in line emission trace the matter power spectrum with some average bias, $b_i(z)$. The mean line intensity, $\bar{S}_i(z)$, in units of Jy sr^{-1} , can be calculated as

$$\bar{S}_i(z) = \int dn_i \frac{L_i}{4\pi D_L^2} y_i D_A^2, \quad (2)$$

where the integration is taken with respect to n_i , the number of galactic line emitters per cosmological comoving volume element. (The factor y_i is the derivative of the comoving radial distance with respect to the observed frequency, i.e. $y = d\chi/d\nu = \lambda_{i,rest}(1+z)^2/H(z)$, and D_A is the comoving angular distance.)

Finally, the shot noise component of the total line power spectrum—with the same units as the clustering term, namely, $\text{Jy}^2 \text{sr}^{-2} (\text{Mpc h}^{-1})^3$ —takes the form

$$P_{i,i}^{shot}(z) = \int dn_i \left(\frac{L_i}{4\pi D_L^2} \right)^2 (y_i D_A^2)^2. \quad (3)$$

2.1. Calculating IR line volume emissivity

The number density of line emitters and the line luminosity that appear in equations (2) and (3) can be derived by a variety of methods. In earlier papers on intensity mapping of molecular and fine-structure emission lines at high redshift ($z \gtrsim 6$), one approach involved using the dark matter halo mass function in lieu of the line emitter density (and invoking a one-to-one correlation between halos and galaxies, which is not unreasonable at high redshifts). The line luminosity, in turn, could be scaled according to the star formation rate, which was related to halo mass via a proportionality constant comprised of factors that described the fraction of baryons available for star formation, as well as the dynamical timescale for star formation and a duty cycle for emission. While this theoretical model is feasible at high redshift to provide an estimate on the mean intensity \bar{S}_i , we take advantage of the relative wealth of observations of [CII] luminosities in individual galaxies, IR galaxy number counts,

and cosmic star formation rate density at the lower redshifts relevant to this study. To this end, we first employ the empirically-constrained, backwards-evolution model of the IR luminosity function $\Phi(L_{IR}, z)$ from Béthermin et al. (2011) (hereafter B11) to predict the number of galaxies with luminosity L_{IR} at a given redshift in some comoving volume of the Universe per logarithmic luminosity interval, i.e., $\frac{dN(L_{IR}, z)}{dV d\log_{10} L_{IR}}$ or $\frac{dn_{IR}}{d\log_{10} L_{IR}}$. One major drawback of our empirical approach is that it does not allow us to model the bias in a self-contained manner, e.g., such as in the halo model formalism that other predictions, which connect L_{IR} to halo mass, employ.

To convert the infrared luminosity to a line luminosity, we apply the relation for L_i as a function of L_{IR} provided by Spinoglio et al. (2012). The fit in their paper was based on the collection of ISO-LWS observations of local galaxies in Brauer et al. (2008), and is reproduced below for [CII]:

$$L_{[CII]158}(L_{IR}) = (0.89 \pm 0.03) \log_{10} L_{IR} - (2.44 \pm 0.07) \quad (4)$$

Thus, it becomes possible to write the cosmic mean intensity and shot noise of the line, in units of Jy sr^{-1} , as a function of redshift based on the B11 luminosity function and Spinoglio et al. (2012) $L_i - L_{IR}$ relation as

$$\begin{aligned} \bar{S}_i(z) &= \int_{L_{IR, \min}}^{L_{IR, \max}} d\log L_{IR} \Phi(L_{IR}, z) \frac{f_i L_{IR}}{4\pi D_L^2} y D_A^2 \quad (5) \\ P_{i,i}^{shot}(z) &= \int_{L_{IR, \min}}^{L_{IR, \max}} d\log L_{IR} \Phi(L_{IR}, z) \left(\frac{f_i L_{IR}}{4\pi D_L^2} y D_A^2 \right)^2 \quad (6) \end{aligned}$$

where f_i , i.e. $\frac{L_i(L_{IR})}{L_{IR}}$, is the fraction of IR luminosity emitted in line i , as computed from equation (3). In other words, we have written \bar{S}_i and $P_{i,i}^{shot}(z)$ as the first and the second moments of the luminosity function.

It should be noted that the mean line luminosity \bar{L}_i does, in reality, include a contribution from diffuse gas in the intergalactic medium (IGM), yet Gong et al. (2012) estimated that the specific intensity of one of the brightest lines typically observed in galaxies, namely [CII], coming from the IGM ranges from $\sim 10^{-3} \text{ Jy sr}^{-1}$ to $\sim 1 \text{ Jy sr}^{-1}$ for different physical conditions in the ISM at $z = 1$ —a negligible amount compared to the emission from the interstellar medium (ISM) of galaxies.

The resulting mean intensities for a variety of FIR lines are plotted in Figure 1 as a function of redshift and observed wavelength. \bar{S}_i vs λ_{obs} can be interpreted as identifying the dominant source of fluctuations, according to our model, for a given frequency. As a specific example, if the target line of an observation is [OI]63 μm at $z = 1$, it is necessary to distinguish between the target line and interlopers from different redshifts which nonetheless contribute power at the observed frequency. Visbal and Loeb (2010) showed how the cross spectra can be used to differentiate between a target line and a contaminating line (or “bad line”, in their words), since emitters at different redshifts will be spatially uncorrelated. For the observed wavelengths of [CII], however, it is apparent from Figure 2 that, with the exception of contributions from [OIII]88 μm near $z \sim 0.01$, the [CII]

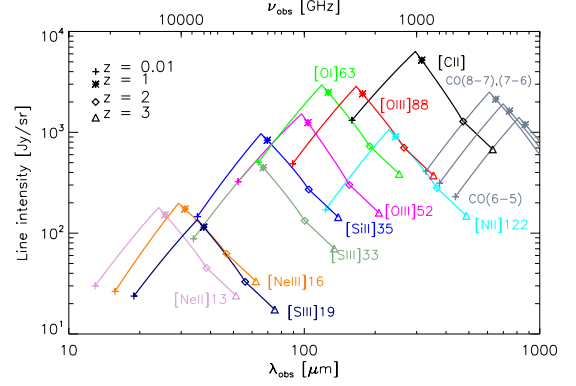


Figure 1. : Intensity of fine structure line emission as a function of observed wavelength for the empirical model based on the B11 luminosity function.

line is not vulnerable to confusion with interlopers.

3. THE [CII] POWER SPECTRUM

3.1. Probing the IR galaxy population

As laid out in Equation 1, $P_{[CII],[CII]}^{clust}$ is sensitive to intensity fluctuations from the full range of normal ($L_{IR} < 10^{11} L_{\odot}$) to ULIRG-class ($L_{IR} > 10^{12} L_{\odot}$) systems because its amplitude is proportional to the mean line intensity, squared. Here, we examine the role of the various luminosity ranges of the constituent IR sources—essentially, the phase space of possible sources that comprise the fluctuations in [CII] emission—on the amplitude of the observed [CII] power.

Suppose a galaxy survey, with a specific detection threshold, $L_{IR, \min}$, aims to observe individual [CII] galaxies in the redshift range from $z = 0$ up to $z = 3$. Figure 3 shows how the observed fraction of $\bar{S}_{[CII]}$ depends on $L_{IR, \min}$ for the empirically-based model described in Section 2.1.

Power spectra at four different redshifts between $z = 0.5$ and $z = 1.5$ comprised of the sources above a few different $L_{IR, \min}$ are represented by Figure 2. In this Figure, we see the clustering amplitude decrease as the IR detection threshold, $L_{IR, \min}$, is raised from $10^8 L_{\odot}$ to $10^{12} L_{\odot}$. (Note that the reduction in the clustering amplitude is precisely the square of the factor of reduction in $\bar{S}_{[CII]}$ plotted in Figure 3.) The level of decrease in clustering power as a result of raising $L_{IR, \min}$ is most dramatic at the lower end of the redshift range of interest, when the luminosity function is represented mostly by normal galaxies and LIRGs. As ULIRGs rise to dominate the IR luminosity function at $z \sim 1.5$, we see that the amplitude of the clustering component of $P_{[CII],[CII]}$ becomes relatively robust until $L_{IR, \min} \sim 10^{12} L_{\odot}$. In fact, we infer from Figure 3 that, at $z = 1.48$, individually resolving galaxies at a depth of 6×10^{11} will recover half of the [CII] light. (For redshifts $z = 0.63, 1.16$ and 3.0 , the corresponding depths to observe half of the [CII] light are $\sim 10^{11}, 2 \times 10^{11}$, and $10^{12} L_{\odot}$, respectively.

3.2. Sensitivity forecast

We present in this section predictions for the [CII] power spectrum with error bar estimates for a feasible experimental platform, namely, a balloon-borne experiment that allows for uninterrupted spectral coverage in

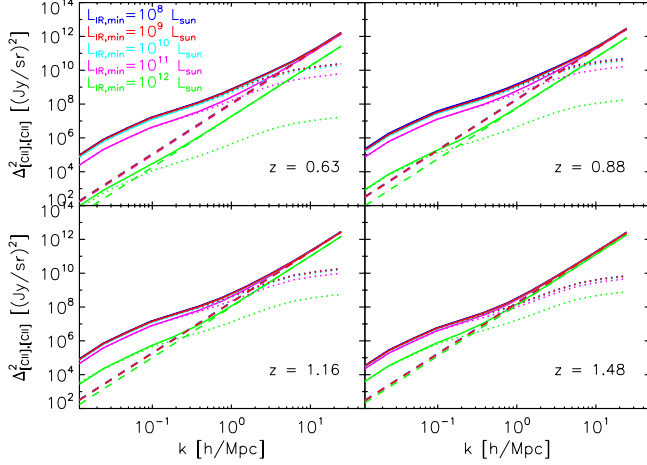


Figure 2 : Predicted [CII] power spectra from $z = 0.63$ to $z = 1.48$. Blue, red, cyan, magenta, and green curves represent the power spectrum computed with a lower limit in the luminosity function corresponding to 10^8 , 10^9 , 10^{10} , 10^{11} , and $10^{12} L_\odot$, respectively.

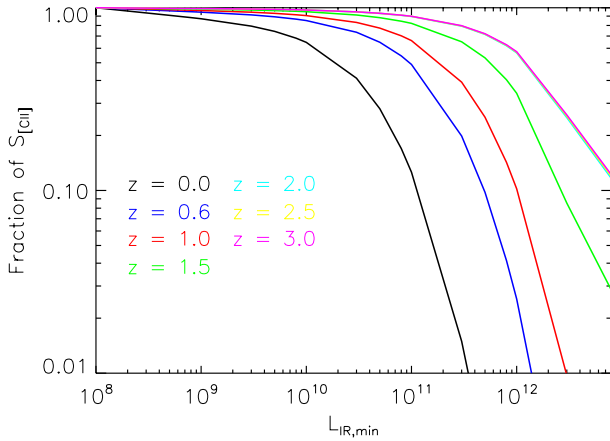


Figure 3 : The fraction of total [CII] mean intensity as a function of lower limit in the luminosity function. Different color curves represent different redshifts, as labeled on the plot.

the wavelength range 240 to 420 μm pertinent to this study. Fiducial experimental parameters are summarized in Table 1. The telescope mirror aperture, D_{ap} , survey area, A_{survey} , and total observing time, t_{obs}^{survey} , are taken as 2.5 m, 1 deg^2 , and 200 hours, respectively, though we explore the effect of varying D_{ap} and A_{survey} on SNR (cf. Figure 5).

Predictions for the fiducial case—as computed from the method of combining the cosmological matter power spectrum and the IR LF model outlined in Section 2.1—for the [CII] power spectrum at four redshifts $z = 0.63, 0.88, 1.16$, and 1.48 are shown in Figure 4. (Note that we use $\Delta^2_{[CII],[CII]} = k^3 P_{[CII],[CII]}(k)/(2\pi^2)$ when plotting the power spectrum. In this notation, the factor k^3 cancels out the volumetric units of $P_{\delta,\delta}(k, z)$ and the integral of $\Delta^2_{[CII],[CII]}$ over logarithmic k bins is equal to

the variance in real space.) At these redshifts, respectively, the average linear bias has been assumed to be $\bar{b} = 2.0, 2.3, 2.6$, and 2.9 , in line with observations from Cooray et al. (2010). The crossing of the one-halo and two-halo terms in the power spectrum can be detected with SNR of order 10 at all redshifts. In calculating the power spectrum sensitivity, the two lowest line-of-sight modes and the lowest transverse mode are not included, since these modes will likely be compromised by the necessity of continuum foreground subtraction and beam-differencing in the fluctuation analysis. The exact effect of continuum subtraction will need to be modeled via simulation.

Error bar estimates and the total SNR for the power spectrum are calculated by assuming a spectrally flat noise power spectrum, so that the noise power in each pixel, P_N , is written as

$$P_N = \sigma_N^2 \frac{V_{pix}}{t_{pix}}, \quad (7)$$

where σ_N^2 is the instrument sensitivity (noise equivalent intensity, or NEI, in units of $\text{Jy sr}^{-1} \text{s}^{1/2}$), V_{pix} is the volume of a pixel, and t_{obs}^{pix} is the time spent observing on a single pixel. The variance of a measured k , $\sigma^2(k)$, is then written as

$$\sigma^2(k) = \frac{(P_{[CII],[CII]}(k) + P_N(k))^2}{N_{modes}}, \quad (8)$$

where N_{modes} is the number of wavemodes that are sampled for a given k bin of some finite width $\Delta \log(k)$. (We have chosen $\Delta \log(k) = 0.3$ for this analysis.)

The total SNR, in turn, is calculated from the expression

$$SNR_{tot} = \sqrt{\sum_{bins} \left(\frac{P_{[CII],[CII]}(k)}{\sigma(k)} \right)^2} \quad (9)$$

It is possible to rewrite P_N in terms of the parameters from Table 1, giving

$$\begin{aligned} P_N &= \left(\sigma_N^2 A_{pix} \Delta r_{los}^{pix} \right) / \left(\frac{t_{survey}}{n_{beams}/N_{instr}^{spatial}} \right) \\ &= \left(\sigma_N^2 A_{pix} \Delta r_{los}^{pix} \right) / \left(\frac{t_{survey} N_{instr}^{spatial}}{A_{survey}/A_{pix}} \right) \\ &= \sigma_N^2 \frac{\Delta r_{los}^{pix} A_{survey}}{t_{survey} N_{instr}^{spatial}} \end{aligned} \quad (10)$$

In this form, it becomes apparent that—with fixed number of spatial pixels, spectral resolution, and total observing time—the only factor driving up the amplitude of noise power is the survey area; the effect of increasing aperture only allows access to higher wavenumbers, which can be useful for subtracting the shot noise from the total power in later steps of data analysis. This behavior is shown clearly in Figure 5, where the SNR is plotted as a function of k for different survey geometries and both mirror diameters.

Table 1: Fiducial Parameters for Envisioned Balloon Experiment

$R = \nu_{obs}/\delta\nu$	450			
t_{obs}^{survey} (hr)	200			
D_{ap} (m)	2.5			
A_{survey} (deg ²)	1.0			
z	0.63	0.88	1.16	1.48
$\bar{S}_{[CII]}$ (Jy sr ⁻¹)	4.56×10^3	6.33×10^3	4.05×10^3	2.55×10^3
NEI (10^7 Jy sr ⁻¹ sec ^{1/2})	3.4	2.1	1.5	1.0
Line Sensitivity (10^{-17} W m ⁻² sec ^{1/2})	1.58	1.13	0.92	0.71
Wavelength Range (μ m)	240-276	276-317	317-365	365 - 420
$\delta\nu$ (GHz)	2.58	2.25	1.95	1.70

3.3. Measuring $\bar{S}_{[CII]}(z)$

To avoid missing the fainter systems when quantifying the mean [CII] intensity, and thus ensure a complete view of the extragalactic [CII]-emitting populations, we introduce intensity mapping as a means of measuring $\bar{S}_{[CII]}$ and its evolution across cosmic time. In order to successfully extract $\bar{S}_{[CII]}$ from the power spectrum, then, it is necessary to divide out $P_{\delta,\delta}(k, z)$ and $\bar{b}_{[CII]}^2(z)$. (High sensitivity on shot noise-dominated modes ensures that the preliminary step of accurate shot noise subtraction is readily attainable.) The confidence with which these are *a priori* known quantities becomes lower as k increases. For example, the 1-halo power spectrum for DSFGs appears to be dependent on L_{IR} of the contributing sources (Viero et al. 2012), indicating the need to map sufficiently wide areas that access k modes where the power is largely independent of the level of 1-halo power.

Returning to Figure 5, we see that, for the purpose of measuring $\bar{S}_{[CII]}$ with the fiducial survey of 1 deg², there are two k bins, namely, $k = 0.16$ and 0.27 h/Mpc in which the 2-halo clustering accounts for at least 75% of the total power. (Surveys with $A_{survey} = 5.3$ and 10 deg², also shown in Figure 5, are wide enough to have three k bins available in the linear regime, but the sensitivity on the additional mode with $t_{obs}^{survey} = 200$ hours is marginal.)

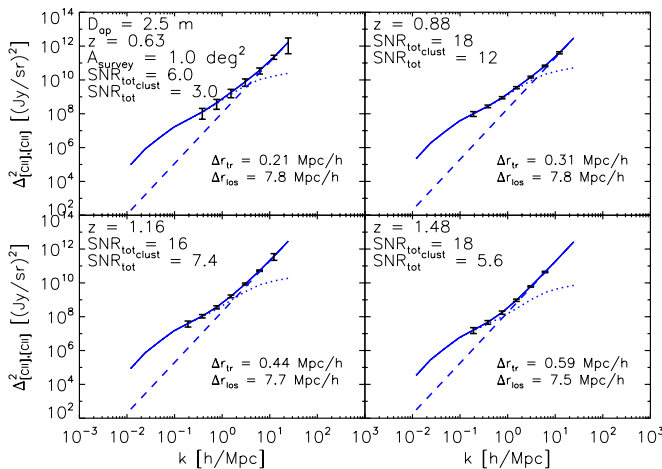


Figure 4. : Predicted [CII] power spectra with error bar estimates from $z = 0.63$ to $z = 1.48$ for telescope with 2.5 meter aperture and a survey area of 1 square degree. Dotted curves indicate power from clustering (including contributions from linear and nonlinear terms), and dashed curves indicate the contribution from shot noise power.

Thus, in considering the case of $A_{survey} = 1.0$ deg², we find that it is possible to measure $\rho_{[CII]}(z)$ within $\sim 10\%$ accuracy from $z = 0.63$ to $z = 1.48$, as shown in Figure 6, where the fractional uncertainty on $\bar{S}_{[CII]}(k, z)$ has been calculated as half the fractional uncertainty on $P_{[CII],[CII]}(k, z)$. In Figure 6, we also include, for comparison, an estimate for $\rho_{[CII]}(z)$ based on the analytic fit to SFRD(z) provided by Hopkins & Beacom (2006) and a constant ratio of 0.003 between $L_{[CII]}$ and L_{IR} . (We use the correlation between SFRD and infrared luminosity described in Kennicutt (1998).) This simple-minded prescription likely overestimates the true [CII] luminosity at redshifts $z \gtrsim 1$, due to the observed [CII] deficiency in ULIRGs, which dominate the IR luminosity density at these redshifts.

4. OBSERVATIONAL STRATEGY

Now let us turn to a question regarding the motivation for intensity mapping in general, as well as in the specific case of [CII] at the redshifts relevant to this study. Having identified the galaxy redshift surveys as an alternative method to measure the 3D clustering power spectrum, it is natural to ask: In which regime does intensity mapping measure the power spectrum with higher SNR than the traditional galaxy surveys?

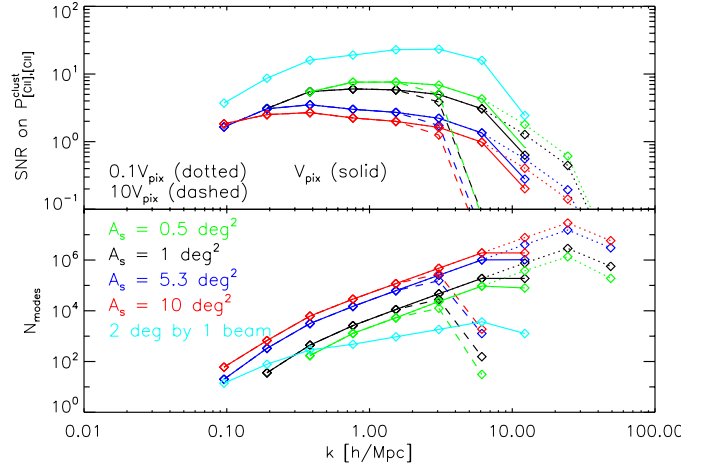


Figure 5. : Signal-to-noise on the clustering term of the [CII] power spectrum $P_{[CII],[CII]}^{clust}$ and number of modes as a function of k at $z = 0.88$. The black, blue, and red lines correspond to survey areas of 1.0, 5.3, and 10.0 deg², respectively. Telescopes with apertures yielding 0.1, 1, and 10 times the fiducial pixel volume, V_{pix} , are shown as the dotted, solid, and dashed lines, respectively.

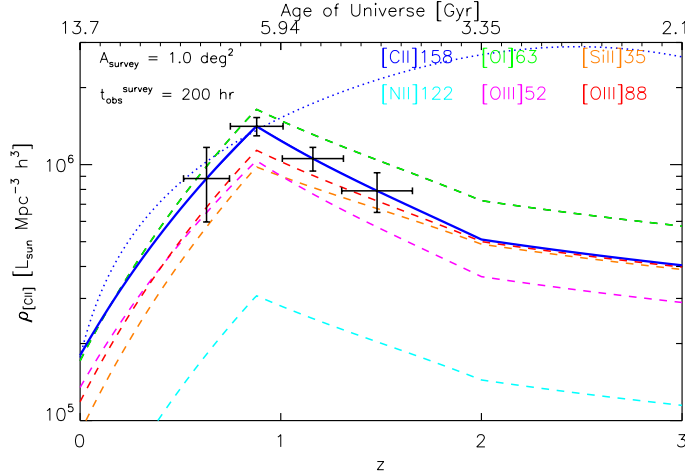


Figure 6. : Error bar estimates on $\rho_{[\text{CII}]}$, as measured by the fiducial experiment, at observed redshifts $z = 0.63, 0.88, 1.16$, and 1.48 . Errors in z correspond to the redshift space spanned by the spectrometer bandwidth. The solid blue curve is the underlying model for $[\text{CII}]$ mean intensity. The luminosity density of other bright IR lines are shown as the dashed colored curves, and the dotted curve is an estimate for $\rho_{[\text{CII}]}$ based on the fit to $\text{SFRD}(z)$ provided by Hopkins & Beacom (2006) and a constant ratio of $L_{[\text{CII}]}$ to L_{IR} equal to 0.003.

The expressions for SNR on a k bin of interest for galaxy and intensity mapping surveys (denoted, respectively, by the subscripts “GS” and “IM”) are

$$\text{SNR}_{\text{GS}} = \frac{\sqrt{N_{\text{modes}}}}{1 + 1/(b_i^2 P_{\delta, \delta} \bar{n}_{\text{gal}})} \quad (11)$$

$$\text{SNR}_{\text{IM}} = \frac{\sqrt{N_{\text{modes}}}}{1 + P_N / (\bar{S}_i^2 b_i^2 P_{\delta, \delta})} \quad (12)$$

To facilitate our comparisons in what follows, we employ toy models for the IR LF (Figure 7) written in the Schechter formalism—parametrized by the usual α , L_* , and ϕ_* —and normalize the total luminosity density to the empirical model from Section 2 (cf. Appendix for details). We stress that these Schechter models are not intended to represent a real interpretation of the distribution of galaxies, but are merely helpful for illustrating the effect of the LF *shape* on the relative usefulness of intensity mapping and traditional galaxy surveys.

The line sensitivity, S_γ (units of $\text{W m}^{-2} \text{s}^{1/2}$), is the figure of merit for detecting an unresolved line in a point source, and we define individual detections at the 5σ level as having a flux above the instrumental noise in a pixel, i.e., above $5 \times S_\gamma t_{\text{pix}}^{-1/2}$. (For this analysis, we have assumed the galaxy surveys have reliable spectroscopic redshifts and thus neglect the problem of confusion noise.)

Since the intensity mapping technique contains information in the power spectrum from sources below a given S_γ , we expect that regimes in which the majority of galaxies are too faint to be resolved are better-suited for intensity mapping observations than observations via the traditional galaxy survey.

One such regime is when the bulk of the galaxy number density at a certain redshift is comprised of galaxies with

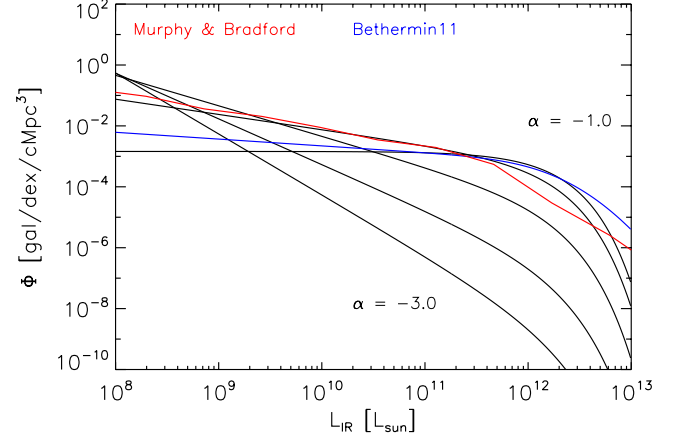


Figure 7. : Toy model IR luminosity functions with faint-end slope (from top to bottom) $\alpha = -1.0, -1.5, -2.0, -2.5, -3.0$. The B11 and Murphy & Bradford models are plotted as blue and red curves, respectively, for comparison.

sub- L_* luminosities (i.e., for steep slope α in the LF). Indeed, this case is illustrated in the middle and righthand panels of Figure 8, where, for LFs with $\alpha < -1.5$, the intensity mapping method (magenta curve) has higher SNR than the corresponding galaxy survey performed with the same instrument (dashed black curve), for all survey observing times. (Note the galaxy survey and intensity mapping survey map the same fiducial area in this example.) However, for the flattest faint-end slope ($\alpha = -1$, lefthand panel), both techniques have comparable SNR for most observing times. We point out that $\text{SNR}_{\text{IM}} > \text{SNR}_{\text{GS}}$ for very short and very long observing times, which correspond to shot-noise dominated and cosmic variance-dominated regimes, respectively, for the galaxy surveys. Also, note that SNR_{GS} and SNR_{IM} have the opposite behavior with steepening α . The intensity mapping technique is not degraded by a steepening of the luminosity function because it does not rely on individual detections. In our model, SNR_{IM} is actually enhanced due to the unmitigated $[\text{CII}]$ emission in normal galaxies (versus ULIRG-class galaxies that are deficient in $[\text{CII}]$).

Figure 8 also shows the effect of changing pixel area by a factor ϵ —due to a change in the telescope’s aperture diameter by $\epsilon^{-1/2}$ —on the SNR. Because the area of the survey is fixed, the transformation on pixel area leads to a change in S_γ by the same factor ϵ , but will not alter P_N (as seen previously in Eq. 10) for the intensity mapping experiment; SNR_{IM} of large-scale clustering modes is robust to changes in pixel area. Thus, the instruments with smaller pixels (triple-dot dashed curve, $\epsilon = 0.1$) achieve greater depths than their large pixel counterparts (dot-dashed curve, $\epsilon = 10.0$), and thus attain higher SNR by resolving more galaxies. Meanwhile, galaxy surveys with large pixels find themselves in the disabling condition of having many sources that are below the detection threshold in a single voxel. Whether or not the galaxy survey experiments with small pixel area outperform the intensity mapping experiment is, however, dependent on the faint-end slope of the luminosity function.

In Figure 9, SNR_{GS} is broken down in terms of the

number of 5σ detections (left panel) and the observed [CII] luminosity density, $\rho_{[CII],obs}$, relative to the total [CII] luminosity density, $\rho_{[CII]}$ (right panel). While it is possible to reach $SNR_{GS} \sim 10$ with ~ 100 galaxies in 200 hours with the fiducial instrument and survey area, the actual fraction of [CII] emission supplied by these detected galaxies is close to 20%. To recover 50% or greater of $\rho_{[CII]}$, one must observe for longer than several thousand hours. (For LF with slopes steeper than $\alpha = -1.0$, the required observing times are significantly longer due to the larger population of faint galaxies.) If, however, one extracts the aggregate, unresolved emission from [CII] via the intensity mapped power spectrum, one is essentially measuring $\frac{\rho_{[CII],obs}}{\rho_{[CII]}} = 1$ as soon as SNR_{IM} on the linear clustering term of the power spectrum is sufficiently high, which we depict in Figure 6 for a 5.3 deg^2 survey with $t_{obs}^{survey} = 1,000 \text{ hr}$.

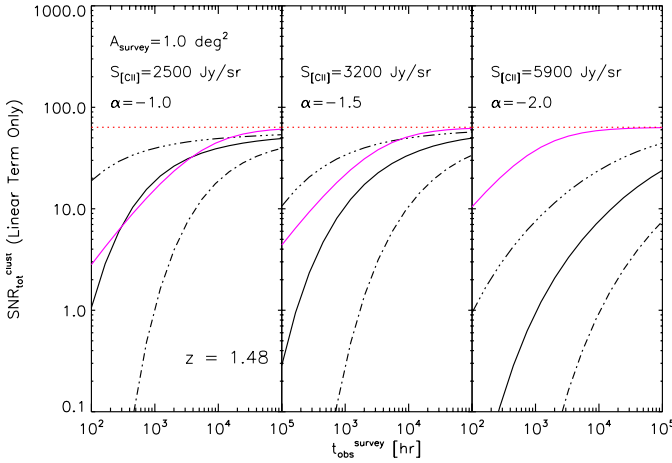


Figure 8 : Total Signal-to-Noise ratio (SNR_{tot}) on the linear portion of the clustering power spectrum of [CII] at $z = 1.5$ as a function of the survey observing time (in hours). SNR_{tot} as computed from intensity mapping—which depends only on the integral of the luminosity function, and not the shape—and from the Schechter function models are plotted. Magenta curves represent the intensity mapping experiment. Black Triple-dot-dashed, dashed, and dot-dashed lines correspond to galaxy survey experiments with pixel volumes 0.1, 1.0, 10.0 times the fiducial value. The horizontal dotted red line is the maximum SNR, set by the number of modes in the survey volume. Note that the mean [CII] intensity is increasing for decreasing faint-end slopes, which is a consequence of fixing the total IR light for a given Schechter model to the B11 value, and then applying the $L_{[CII]} - L_{IR}$ relation to predict [CII] luminosity.

It is important to note that the fractional errors, defined as $f_{err} \equiv \sigma_N / \left(\sqrt{t_{obs}^{pix}} \bar{S}_{[CII]} \right)$, corresponding to the observing times plotted in Figures 8 and 9 are in the range of ~ 300 to 10 , which do not provide insight into the case of low fractional errors achievable by futuristic space telescopes, for example. In this latter regime of high sensitivity observations, we expect the galaxy surveys to be successful in detecting a large number of

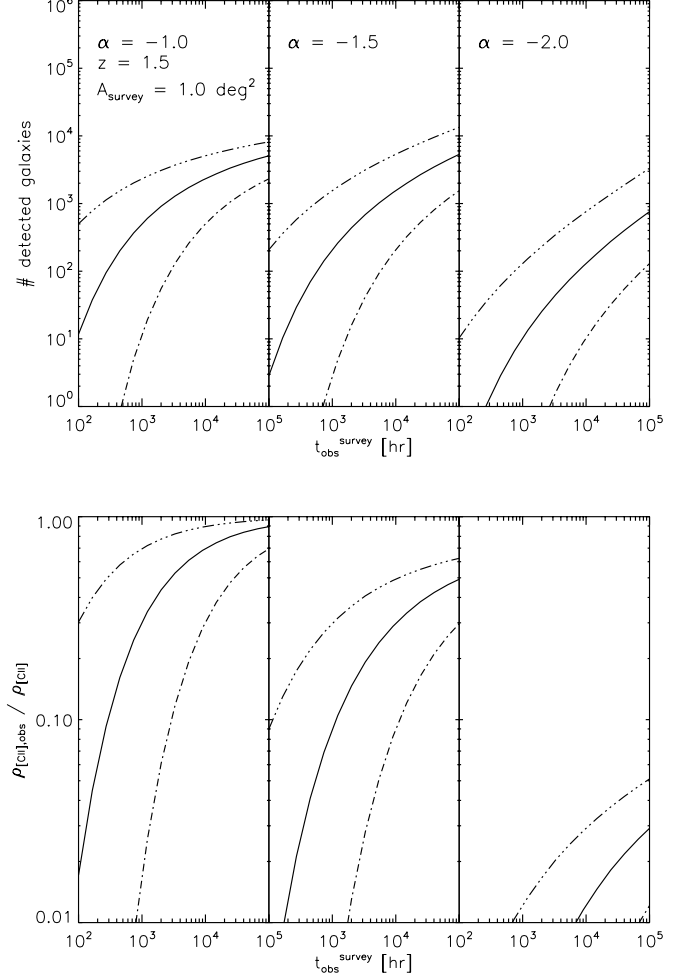


Figure 9 : The predicted number of [CII]-detected galaxies and observed fraction of [CII] luminosity density as a function of survey time for the square degree field. Solid, dash-triple-dotted, and dash-dotted curves represent the fiducial V_{pix} , $0.1V_{pix}$, and $10V_{pix}$, resp.

sources in the full spectrum of faint to bright sources. As a concrete example, we include in the comparison between intensity mapping and galaxy surveys a futuristic experiment aboard a cold space telescope, changing only the achievable NEI in our set of fiducial parameters. For a 6 K telescope with 4% emissivity, in a single polarization, 25% instrument transmission, we use in the following analysis an NEI of $4.3 \times 10^5 \text{ Jy sr}^{-1} \text{ sec}^{1/2}$ at $393 \mu\text{m}$. (The fractional errors corresponding to such an NEI in the range of observing times from $t_{obs}^{survey} = 100$ to 10^5 hr are $f_{err} = 0.1$ to 10 .) The top panel of Figure 10 summarizes—for two representative Schechter functions—the relative performance of each observational method in terms of the SNR on the large scale modes of the power spectrum as a function of observing time. The number of [CII]-detections and the fraction of [CII] light recovered by the galaxy survey are shown in the lower two panels, respectively. From this figure, it is clear that such a low-noise galaxy survey experiment supersedes intensity mapping surveys as an effective probe of the majority of the galaxy population in the case of a flat IR luminosity function, which

is likely the case at $z = 1.5$. On the other hand, we find that SNR_{IM} is, as in Figure 8, not degraded, but enhanced in the case of $\alpha = -2.0$.

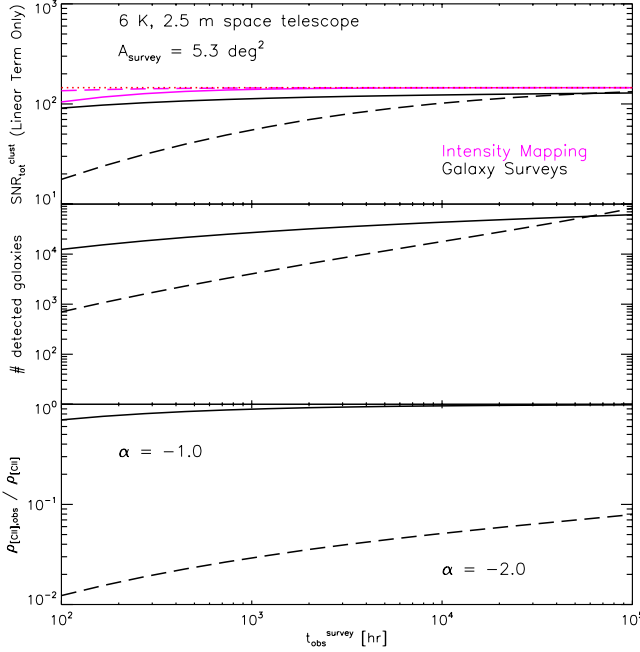


Figure 10. : *Top panel:* Total $\text{SNR}(t_{obs}^{survey})$ on the linear portion of the [CII] clustering power spectrum for intensity mapping (magenta curves) and galaxy survey (black curves) experiments performed with the cold space telescope described in the main text. Solid and long-dashed curves represent luminosity with $\alpha = -1.0$ and -2.0 , resp. *Middle panel:* Number of detected galaxies as a function of survey time for the galaxy survey. *Bottom panel:* Observed fraction of [CII] luminosity density as a function of survey time.

5. DISCUSSION

As noted in Section 4, galaxy surveys performed using instruments with small telescopes and large pixels fare worse in the detection of individual galaxies, and,

hence, in measuring the power spectrum compared to intensity mapping experiments using an identical instrument. Another regime where galaxy surveys find themselves in the large-pixel limit is at high-redshift, and so the early studies of [CII] intensity mapping during Reionization are, indeed, well-motivated in this regard. Not to mention, there is also strong evidence for steep ($\alpha \sim -2$) luminosity functions in the rest frame UV at $z \sim 7$ (Bouwens et al. 2014), which additionally positions intensity mapping experiments as better-suited probes of the power spectrum and the aggregate galaxy population than galaxy redshift surveys. Although beyond the scope of this paper, our findings here reinforce the notion that the $z > 6$ Universe presents an ideal opportunity to learn about galaxy populations via intensity mapping

should mention also future NASA FIR surveyor missions (SAFIR?)

6. SUMMARY

We have presented predictions for the measurement of the [CII] power spectrum between $0.63 < z < 1.48$, and demonstrated the detectability of the power spectrum in both clustering and shot noise terms in this redshift range. Fluctuations of [CII] intensity have been modeled by combining empirically-constrained estimates of the [CII] luminosity from the B11 IR luminosity function and Spinoglio et al $L_i - L_{IR}$ relations with the theorized dark matter power spectrum. On large scales, the fact that the clustering amplitude of [CII] fluctuations is proportional to the mean [CII] intensity indicates the potential for measuring cosmic evolution of aggregate [CII] emission with the line intensity mapping approach. For the fiducial experiment considered in this paper, we have found that it would be possible to measure the [CII] luminosity density with fractional errors on the order of 10%. In examining the effect of luminosity function shape, telescope aperture, and fractional error (or instrument noise level) on the relative performances of intensity mapping to galaxy surveys, we have further demonstrated that, in the case where experiments with low fractional errors are not feasible, intensity mapping experiments always outperform galaxy redshift surveys when measuring the mean [CII] intensity, and, for steep luminosity functions, the clustering power spectrum, as well.

APPENDIX

To explore the effect of the luminosity function shape on the relative performances of intensity mapping and galaxy surveys in observing the [CII] power spectrum and mean intensity of [CII] emitters, we have introduced toy models to represent different $\Phi(L_{IR}, z) \equiv \frac{dN}{dL_{IR}dV}$.

We parametrize our luminosity function as a Schechter function

$$\Phi(L_{IR}, z)dL_{IR} = n_* \left(\frac{L_{IR}}{L_*} \right)^\alpha \exp \left(-\frac{L_{IR}}{L_*} \right) d \left(\frac{L_{IR}}{L_*} \right) \quad (1)$$

where n_* is the normalization for number density, L_* is the characteristic luminosity at the knee, and α is the faint-end slope, as usual.

Power-law luminosity functions are notoriously ill-behaved if the lower limit of integration for either the luminosity functions or its moments is extended to zero. Rather than implement a break in the power law, we simply cut it off at some $L_{IR,min}$ and choose to fix in our analysis the total IR luminosity density from galaxies as predicted by B11, denoted as ρ_{IR}^{B11} , such that

$$\int d\left(\frac{L_{IR}}{L_*}\right) n_* L_* \left(\frac{L_{IR}}{L_*}\right)^{\alpha+1} \exp\left(-\frac{L_{IR}}{L_*}\right) \equiv \rho_{IR}^{B11} \quad (2)$$

This is motivated by the observation that in many cases we do have constraints on the integrated light (from, for example, the cosmic infrared background or from the cosmic star formation rate density or the requirement of critical reionization), whereas we may not in general have detailed constraints on the distribution of light among galaxies, i.e., the shape of luminosity function.

The number density of sources, n , can, in turn, be computed from

$$n = \int d\left(\frac{L_{IR}}{L_*}\right) n_* \left(\frac{L_{IR}}{L_*}\right)^{\alpha} \exp\left(-\frac{L_{IR}}{L_*}\right) \quad (3)$$

Finally, equation 2 allows us to calculate the [CII] luminosity density for each IR-normalized toy model as

$$\rho_{[CII]} = \int d\left(\frac{L_{IR}}{L_*}\right) n_* L_* \left(\frac{L_{IR}}{L_*}\right)^{\alpha} f_{[CII]} L_{IR} \exp\left(-\frac{L_{IR}}{L_*}\right) \quad (4)$$

where $f_{[CII]}$ is the fraction of IR luminosity emitted in [CII], or $\frac{L_{[CII]}(L_{IR})}{L_{IR}}$, described by the Spinoglio relations. Because $L_{[CII]}$ is slightly sublinear in L_{IR} , it follows that the toy models with steep faint-end slopes will produce more [CII] emission than their flatter counterparts.

REFERENCES

- B  thermin, M., Dole, H., Lagache, G., Le Borgne, D., & Penin, A. 2011, A&A, 529, A4
 Bouwens, R. J. et al. 2014, ArXiv e-prints
 Brauher, J. R., Dale, D. A., & Helou, G. 2008, ApJS, 178, 280
 Burgarella, D. et al. 2013, A&A, 554, A70
 Cooray, A. et al. 2010, A&A, 518, L22
 de Putter, R., Holder, G. P., Chang, T.-C., & Dore, O. 2014, ArXiv e-prints
 D  az-Santos, T. et al. 2013, ApJ, 774, 68
 Dole, H. et al. 2006, A&A, 451, 417
 Glenn, J. et al. 2010, MNRAS, 409, 109
 Gong, Y., Cooray, A., Silva, M., Santos, M. G., Bock, J., Bradford, C. M., & Zemcov, M. 2012, ApJ, 745, 49
 Gong, Y., Cooray, A., Silva, M. B., Santos, M. G., & Lubin, P. 2011, ApJ, 728, L46
 Graci  -Carpio, J. et al. 2011, ApJ, 728, L7
 Hopkins, A. M. & Beacom, J. F. 2006, ApJ, 651, 142
 Kennicutt, Jr., R. C. 1998, ApJ, 498, 541
 Lidz, A., Furlanetto, S. R., Oh, S. P., Aguirre, J., Chang, T.-C., Dor  , O., & Pritchard, J. R. 2011, ApJ, 741, 70
 Morales, M. F. & Wyithe, J. S. B. 2010, ARA&A, 48, 127
 Parsons, A. R. et al. 2013, ArXiv e-prints 1304.4991
 Planck Collaboration et al. 2013, ArXiv e-prints
 Pullen, A., Dore, O., & Bock, J. 2013, ArXiv e-prints
 Sargsyan, L. et al. 2012, ApJ, 755, 171
 Smith, R. E. et al. 2003, MNRAS, 341, 1311
 Spinoglio, L., Dasyra, K. M., Franceschini, A., Gruppioni, C., Valiante, E., & Isaak, K. 2012, ApJ, 745, 171
 Switzer, E. R. et al. 2013, MNRAS, 434, L46
 Tingay, S. J. et al. 2013, Journal of Physics Conference Series, 440, 012033
 Viero, M. P. et al. 2012, ArXiv e-prints
 Visbal, E., Trac, H., & Loeb, A. 2011, J. Cosmology Astropart. Phys., 8, 10

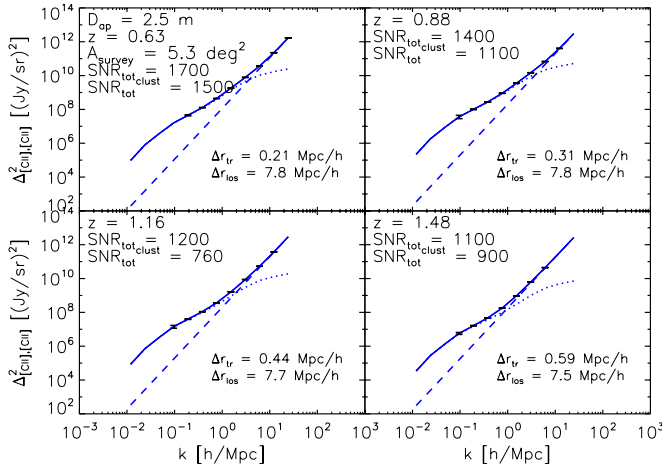


Figure 11. : Same as previous figure, except for the space telescope and 5 square degree survey area.

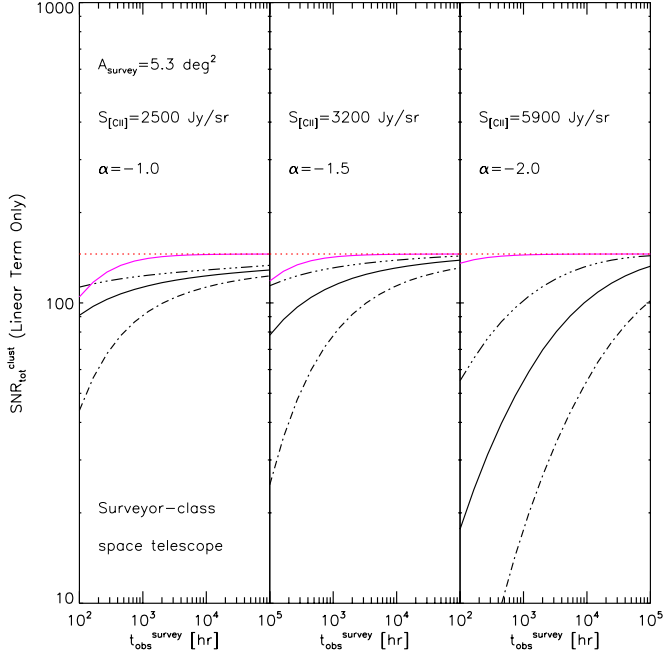


Figure 12. : Same as previous figure, except for the space telescope and 5 square degree field.

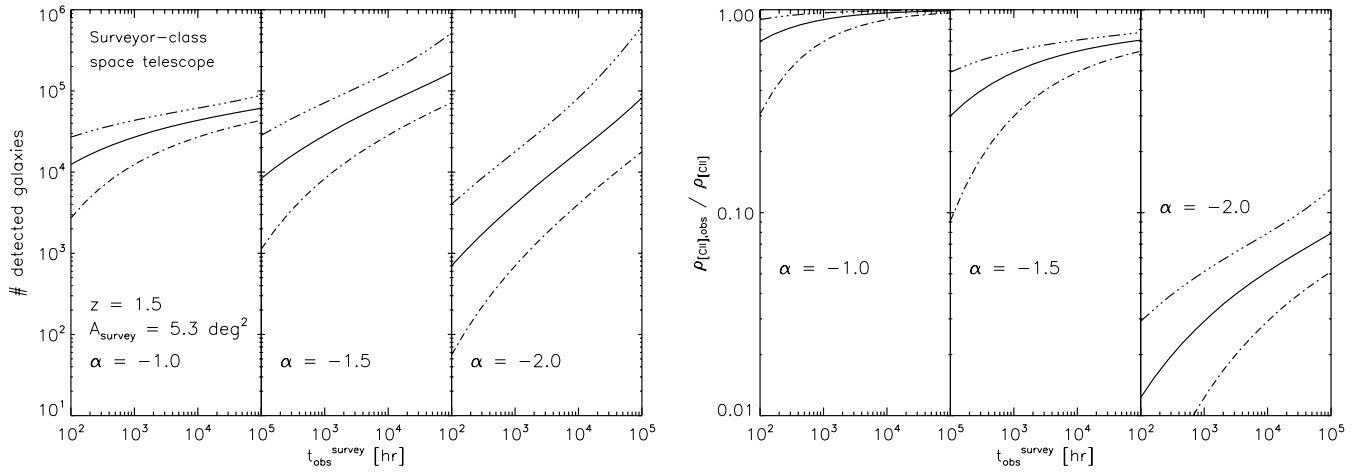


Figure 13. : Same as previous figure, except for the space telescope and 5 square degree field.